Article

Characterization of Ceramic Thermal Shock Cracks Based on the Multifractal Spectrum

Changxu Shao [1,2]**, Hao Guo** [3,]*****[,] **Songhe Meng** [4]**, Yingfeng Shao** [5]**, Shanxiang Wang** [1]**, Shangjian Xie** [1] **and Fei Qi** [1,]*****

1   School of Mechanical and Electric Engineering, Soochow University, Suzhou 215021, China
2   School of Mechanical Engineering and Automation, Zhejiang Sci-Tech University, Hangzhou 310018, China
3   Jiangsu Provincial Key Laboratory of Advanced Robotics & Robotics and Microsystems Center,
    Soochow University, Suzhou 215021, China
4   National Key Laboratory of Science and Technology on Advanced Composites in Special Environments,
    Harbin Institute of Technology, Harbin 150001, China
5   State Key Laboratory of Nonlinear Mechanics, Institute of Mechanics, Chinese Academy of Sciences,
    Beijing 100190, China
*   Correspondence: hguo@suda.edu.cn (H.G.); qifei@suda.edu.cn (F.Q.)

Abstract: Ceramics are commonly used as high-temperature structural materials which are easy to fracture because of the propagation of thermal shock cracks. Characterizing and controlling crack propagation are significant for the improvement of the thermal shock resistance of ceramics. However, observing crack morphology, based on macro and SEM images, costs much time and potentially includes subjective factors. In addition, complex cracks cannot be counted and will be simplified or omitted. Fractals are suitable to describe complex and inhomogeneous structures, and the multifractal spectrum describes this complexity and heterogeneity in more detail. This paper proposes a crack characterization method based on the multifractal spectrum. After thermal shocks, the multifractal spectrum of alumina ceramics was obtained, and the crack fractal features were extracted. Then, a deep learning method was employed to extract features and automatically classify ceramic crack materials with different strengths, with a recognition accuracy of 87.5%.

Keywords: ceramics; thermal shocks; crack propagation; multifractal spectrum; deep learning

MSC: 74A40; 74E99; 74A45; 28A80; 68T07

1. Introduction

Ceramic materials are often used as high-temperature structural materials. In extreme high-temperature environments, ceramic materials need to withstand complex loads and environments such as force and stress cycling, environmental media erosion and scouring, and thermal shocks [1]. Due to the inherent brittleness of ceramics, the thermal stresses caused by temperature differences during rapid warming or thermal shock from high temperatures can lead to the development and rapid propagation of microcracks, resulting in a sudden decay in material strength [2], which seriously affects the reliability of critical thermal protection structures and limits the practical application of ceramic materials as high-temperature materials. The existence and propagation of cracks is the main cause of fracture of brittle materials [3]; therefore, the study of the influence of microcrack propagation on the thermal shock resistance of ceramic materials and the exploration of methods to inhibit the propagation of microcracks are key issues that need to be urgently addressed to improve the thermal shock resistance of ceramics.

Based on the thermal shock fracture theory (TSF) and thermal shock damage theory (TSD), Duan et al. [4] developed a modified thermal shock model that takes into account the variation of material properties with temperature to reveal the thermal shock damage

mechanism of ceramic materials in terms of their temperature characteristics. Luo et al. [5] used ABAQUS finite element software to simulate the generation and propagation of cracks in the indentation zone during microhardness testing of ultrafine crystalline Si_2N_2O-Si_3N_4 ceramics. Li et al. [6] constructed a fine-scale damage mechanics model to simulate the interaction between thermal impact cracks and prefabricated cracks, extending the study of the thermal impact damage mechanism of ceramics. While the mechanisms of crack generation and propagation have been studied above, Qi et al. [7] investigated the effect of thermal shock-induced crack propagation on the residual strength of ceramics in terms of fractal geometry, calculated the fractal dimension of thermal shock cracks by the box-counting method, and explained the relationship between crack length and fractal dimension using the fractal energy of microcrack fractal patterns in quasi-brittle solids. Ricco et al. [8] investigated the effect of microstructure and surface energy on subcritical crack propagation in microcrystalline glass and found that stress corrosion cracking in microcrystalline glass is due to a combination of surface energy and microstructural features. Quan et al. investigated fatigue cracking of metallic materials [9] and fatigue cracking of bonded joints under type I loading [10], and verified that crack expansion causes energy dissipation.

It was found that thermal shock cracks in ceramic materials generally have a fractal structure, and the spatial distribution information of cracks is considered when performing fractal characterization of microcracks. The multifractal spectrum of crack propagation after the thermal shock of ceramic materials was calculated to obtain the complexity of crack propagation and spatial distribution characteristics, which can better characterize the non-regular and non-uniform characteristics of cracks. Zhu et al. [11] used multiple fractals to study random fracture crack networks, providing a possible solution for the study of more complex surface topographies. Ji et al. [12] used multiple fractals to characterize the phase structure of abradable layers on material surfaces and analyze the high-speed scraping behavior of material surfaces. Pan [13] and others used multifractal spectra to make up for the shortcomings of traditional methods in revealing the heterogeneity of crack distribution in describing concrete cracks, verified that multifractal spectra can distinguish the subtle differences between two similar concrete crack distributions, and provided a new idea for assessing the damage of concrete structures. Butenko et al. [14] carried out a multifractal analysis on nitinol glass annealed at different temperatures, counted its surface characteristics, and verified the possibility of detecting system phase transition in crystalline form. Martsepp et al. [15] irradiated pure tungsten samples with high-temperature deuterium plasma at different times and compared the multifractal spectrum of the sample surface with the Fourier spectrum. The multifractal spectrum of the surface can determine the time dependence of surface damage. Feng et al. [16] studied the crack propagation and internal fracture process of coal under dynamic load and verified that the crack propagation and internal fracture surface of coal have multifractal characteristics, indicating that the multifractal characteristics can be used to evaluate the brittleness of coal under dynamic load and predict the coal failure risk of underground coal mines. Jouini et al. [17] used multiple fractals to allow the classification of rock samples according to their degree of inhomogeneity. Astinchap et al. [18] evaluated chest computed tomography (CT) images of 2019 patients with novel coronavirus disease (neo-coronavirus pneumonia) by multiple fractal techniques, and Tsvetkov et al. [19] used multiple fractals to develop a kinetic model of the neo-coronavirus pandemic. This shows that multifractals are widely used in various disciplines.

Multifractals have good application prospects in terms of characterizing the surface characteristics of materials and analyzing the fracture process. Therefore, this paper will extract crack characteristics through a multifractal spectrum. Although multifractal spectra can effectively characterize the cracks, they still need a method to learn these characteristics and to objectively identify similar characteristics. Deep learning has excelled in solving many problems such as image target recognition, speech recognition, and natural language processing, avoiding problems such as the subjective influence of manually extracted features and the limited expressiveness of shallow network structures. Among the various

types of neural networks, convolutional neural networks have been the most intensively studied. The basic structure of a Convolutional Neural Network (CNN) consists of an input layer, a convolutional layer, a pooling layer, a fully connected layer, and an output layer, and the emergence of large-scale labeled data, such as those found on ImageNet, and the rapid improvement of GPU computing performance have advanced the research on convolutional neural networks. In particular, after the introduction of the AlexNet [20] network model in 2012, convolutional neural networks have been developed at a high speed, and subsequent convolutional neural network models such as Visual Geometry Group Network (VGG), GoogleNet, Residual Network (ResNet), etc., have emerged.

Li et al. [21] proposed a new method based on multifractal theory, sequence feature fusion, and an improved probabilistic neural network, which improved the vibration identification performance of the perimeter system of the dual Mach Zehnder interferometer. The feature of the original signal is extracted in the form of multifractal spectra and associated with a probabilistic neural network, which realizes the beneficial fusion of multifractal theory and the probabilistic neural network. Therefore, this paper also integrates multifractal spectra into deep learning algorithms, establishes a correlation model between crack propagation fractal characteristics and the thermal shock damage degree based on multifractal spectra and deep learning, and verifies the validity of the model through thermal shock experiments. The purpose of this study was to realize the combination of nonlinear geometric methods, artificial intelligence methods, and thermal shock damage characterization of composite materials.

2. Materials and Methods

2.1. Thermal Shock Test

The Al_2O_3 ceramic block used in this paper was 50 mm long, 50 mm wide, and 5 mm thick according to Qi's test method [4]. By measuring the size and weight, the density of the ceramic was calculated to be greater than 95%. The ceramic blocks were cut into 5 mm × 10 mm × 50 mm plates and the ceramics were placed in a muffle furnace and heated at a rate of 15 °C/min and held at a preset temperature for 20 min. The samples were then removed from the muffle furnace and immediately placed in water ($\leq$17 °C). After cooling for 10 min, the samples were dried in an 80°C environment for 2 h and stained with blue dye. This test method was used to obtain thermal shock cracks in ceramics at different temperatures.

2.2. Multifractal Spectrum Calculation

The multifractal is a complex fractal structure. It is usually created by introducing a probability distribution function for the fractal structure and calculating its moments of each order, which serve to describe the complexity and inhomogeneity of the fractal structure intuitively and in more detail while obtaining a continuous spectrum of fractal dimensions, which is then called the multifractal spectrum.

The box-counting dimension method is generally used to calculate the multifractal spectrum, as follows [22]:

Define a box of scale $\varepsilon \times \varepsilon$, cover the target image with this box and calculate the pixel n_{ij} of cracks in each box (i, j), divide by the total pixels Σn_{ij} of all cracks to get its probability measure:

$$P_{ij} = n_{ij}/\Sigma n_{ij} \tag{1}$$

Define the collocation function $\varphi_q(\varepsilon)$ as the moment of order q of the probability measure $P_{ij}(\varepsilon)$:

$$\varphi_q(\varepsilon) = \sum P_{ij}^q(\varepsilon) = \varepsilon^{\tau(q)} \tag{2}$$

If the latter equality sign holds, then:

$$\tau(q) = \ln\varphi_q(\varepsilon)/\ln\varepsilon \tag{3}$$

where $\boldsymbol{\tau}(\boldsymbol{q})$ is called the quality index and $\boldsymbol{q}$ is the weighting factor.

From statistical physics theory, the Legendre transformation of $\boldsymbol{\tau}(\boldsymbol{q}), \boldsymbol{q}$ yields:

$$\alpha = d\boldsymbol{\tau}(\boldsymbol{q})/d\boldsymbol{q} \tag{4}$$

$$f(\alpha) = \alpha q - \boldsymbol{\tau}(\boldsymbol{q}) \tag{5}$$

$f(\alpha)$ is the multifractal spectrum of the image, where α is called the singularity index and is the parameter used to describe the strength of the local singularity of a probability measure. $f(\alpha)$ in its physical sense can be understood simply as the fractal dimension of a set with the same α value. For a complex fractal image, it has a series of subsets represented by different α values within it, and different subsets will have the corresponding fractal dimension $f(\alpha)$. These singularity indexes α and their corresponding $f(\alpha)$ then form a spectrum of dimensions describing the properties of multiple fractals, i.e., the multifractal spectrum. The multifractal spectrum of the crack image is calculated by Equations (1)–(5), and the results are shown in Figure 1D.
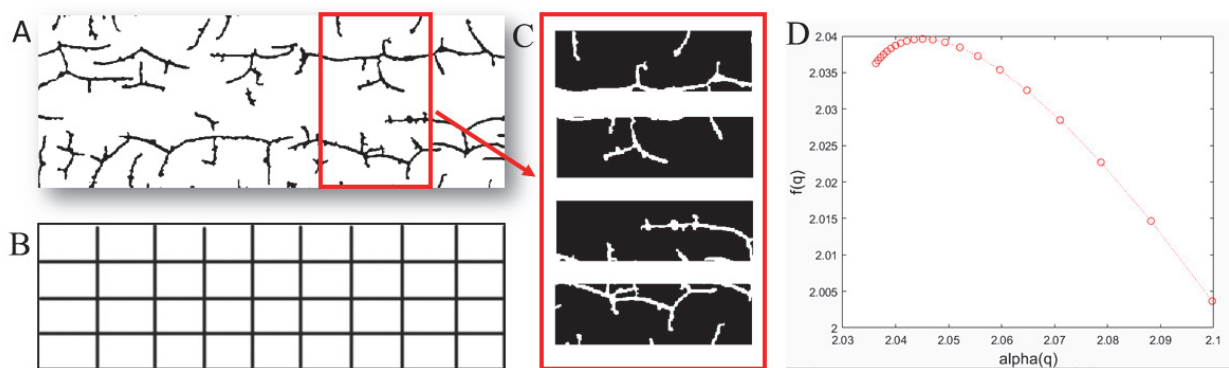

Figure 1. Schematic representation of the multifractal characterizations of the crack propagation: (**A**) pre-processing of the original crack image, (**B**,**C**) dividing cracked images, and (**D**) calculating crack multifractal spectra.

In this paper, each crack image will be cut to extend the amount of data and to combine the non-linear characteristics of the crack with its spatial distribution information. By calculating the crack multifractal spectrum and quantifying the irregular and inhomogeneous shape of crack propagation, we obtain a quantitative characterization of the complexity of microcrack propagation and its spatial distribution, which provides the data required to study the effect of microcrack propagation on thermal impact performance, as shown in Figure 1.

Both α and $f(\alpha)$ will change according to the artificially set weight q. Therefore, we consider analyzing α and $f(\alpha)$ separately, study the relationship between them and the weight q, transform the values of α and $f(\alpha)$ into $\alpha(q)$ and $f(q)$ chromaticity diagrams, explore the pattern between them, and use the chromaticity diagrams of these two to construct a suitable training set and test set for the training and detection of deep learning models.

2.3. Construction of Deep Learning Model

In this paper, the AlexNet model will be used as the framework to build the deep learning model needed for this paper. One of the advantages of the AlexNet model is that it uses ReLU as the activation function of the CNN, which is faster to converge than the traditional Sigmoid and avoids the gradient dispersion problem. In addition, AlexNet applies Dropout to the last few fully connected layers to avoid overfitting the model. In addition, it proposes the LRN layer, which enhances the generalization of the model.

The shallow features of the crack propagation morphology were fused with the spatial distribution of complexity features obtained from multifractal spectroscopy to establish a model between crack propagation features and the degree of thermal shock damage based

on multifractal spectroscopy and deep learning, as shown in Figure 2. The results were classified into four categories based on the ratio of strength values to initial strength values for Al_2O_3 ceramic materials in different cracking cases. The dataset consists of $\alpha(q)$ and $f(q)$ chromaticity maps obtained in the previous section, which were input into the model for training, and a test set was used to check the generalization recognition accuracy of the model.
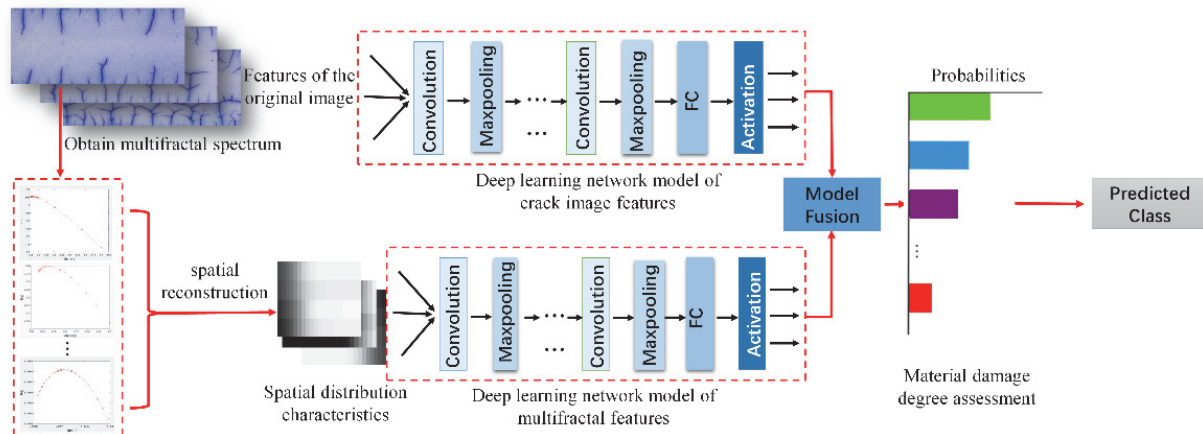

Figure 2. Deep learning-based fusion model between crack propagation characteristics and the thermal shock damage.

3. Results

3.1. Calculation Results of Multifractal Spectrum of Crack Image

Through the thermal shock test, we can obtain the thermal shock crack image of ceramic materials, as shown in Figure 3a, using filtering, erosion, binarization, etc., to pre-process the image, denoising, and retaining the effective information in the image to obtain the image after processing, as shown in Figure 3b.
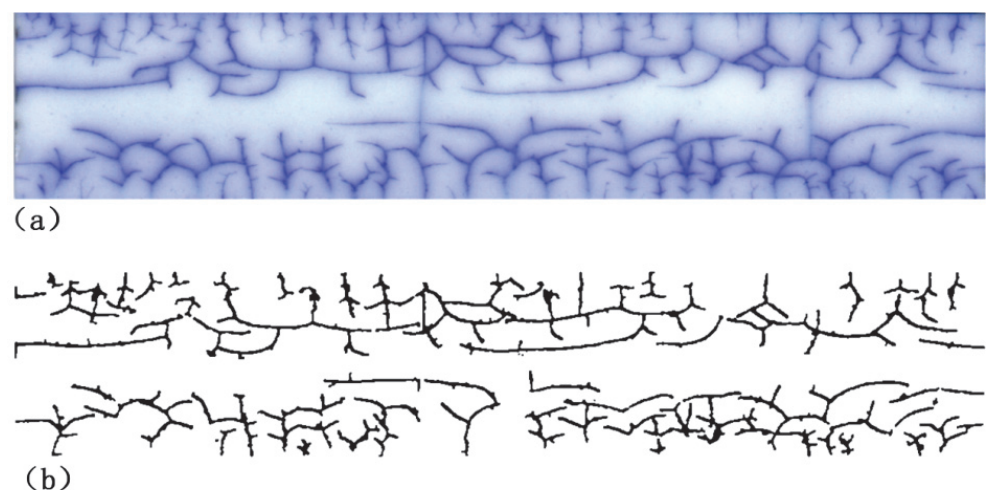

Figure 3. Comparison between the original image and processed image of cracks. (**a**) Original image of cracks. (**b**) Processed image of cracks.

The processed image is input into the multifractal spectrum calculation program, and the multifractal spectrum is calculated for this crack image. The weight factor q is an artificially set parameter, and the paper selects q as $[-1, 1]$, $[-2, 2]$, $[-5, 5]$, and $[-10, 10]$ for discussion (shown in Figure 4), and obtains the multifractal spectrum image with different values of q.
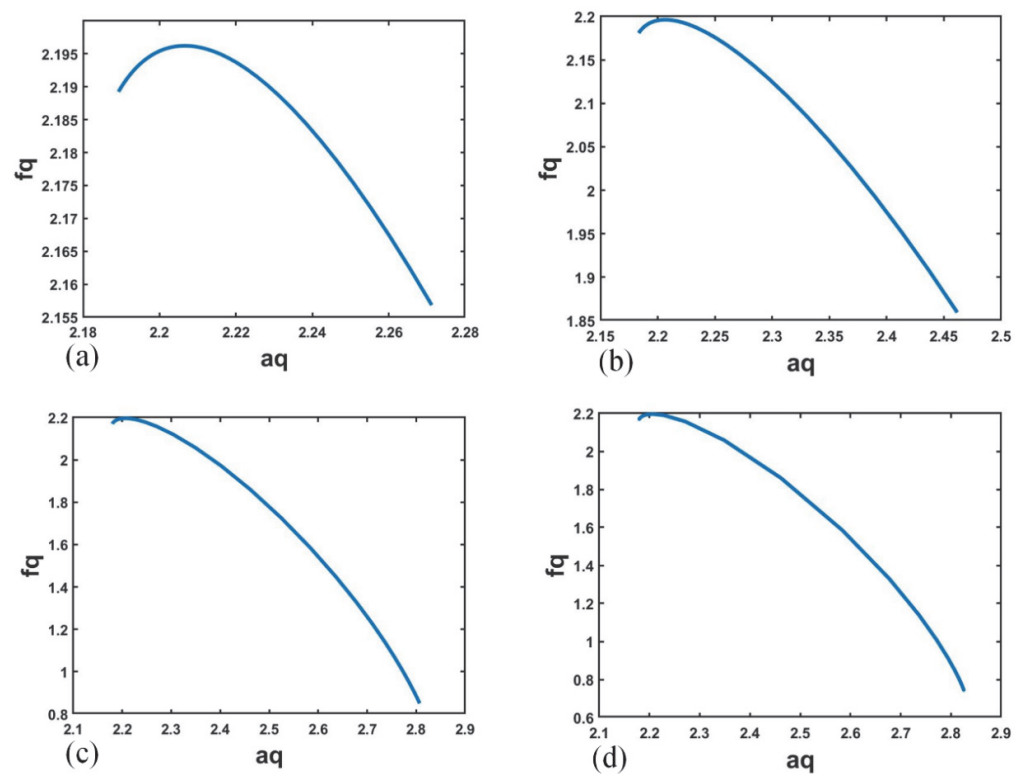
Figure 4. Multifractal spectrum images with different q values: (**a**) $q \in [-1, 1]$. (**b**) $q \in [-2, 2]$. (**c**) $q \in [-5, 5]$. (**d**) $q \in [-10, 10]$.

The horizontal coordinate of the multifractal spectrum image is the singularity index α and the vertical coordinate is the singular spectrum $f(\alpha)$, and both the singularity index and the singular spectrum are functions concerning the weight factor q. Therefore, the weight factor q is taken as the independent variable, $\alpha(q)$ and $f(q)$ are taken as the dependent variables, and their relationship with q is analyzed separately.

To combine the non-linear features of the cracks with information about their spatial distribution and to observe their patterns more intuitively, we cut the crack images and transformed the values of $\alpha(q)$ and $f(q)$ into chromaticity maps. Five copies of the image were cut horizontally and four copies were cut vertically, as shown in Figure 5; the values of $\alpha(q)$ and $f(q)$ were calculated for each small piece, and the values of both were normalized and transformed into a chromaticity map, as in Figure 6 for the first column, for example. Thus, depending on the different values of the weighting factor q, the respective corresponding chromaticity maps of $\alpha(q)$ and $f(q)$ could be obtained, as shown in Figure 7. After the comparison of the results of the subsequent experimental process, the best effect was obtained when q is $[-1, 1]$, so we finally selected the weighting factor q as $[-1, 1]$.
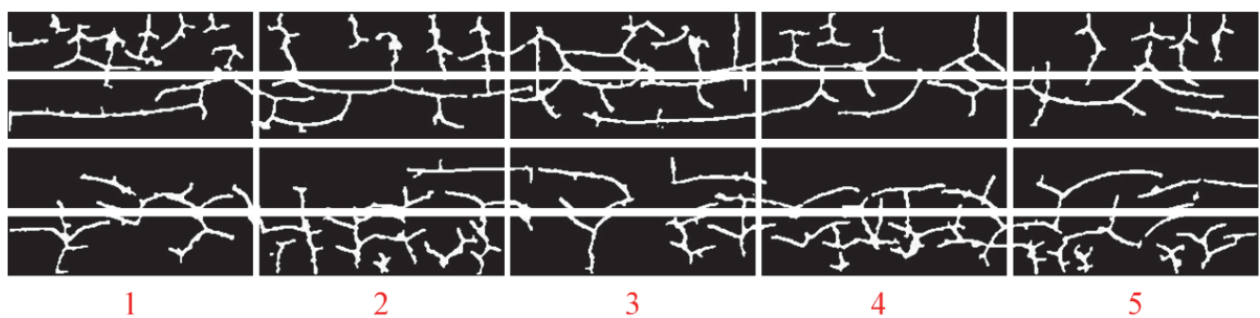

Figure 5. Divide four images horizontally and five images vertically, and calculate the values of $\alpha(q)$ and $f(q)$ of each subimage.
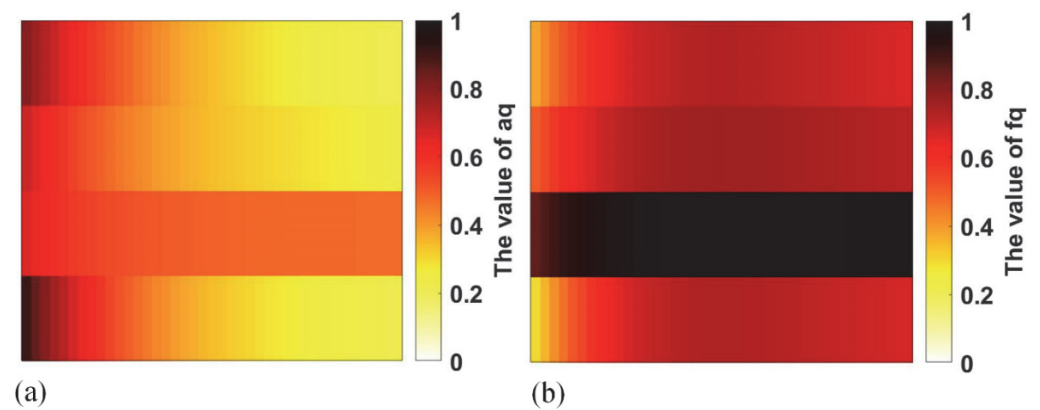
Figure 6. Normalize values of $\alpha(q)$ and $f(q)$, convert them into chromaticity diagrams: (**a**) $\alpha(q)$ and (**b**) $f(q)$ of the first column.
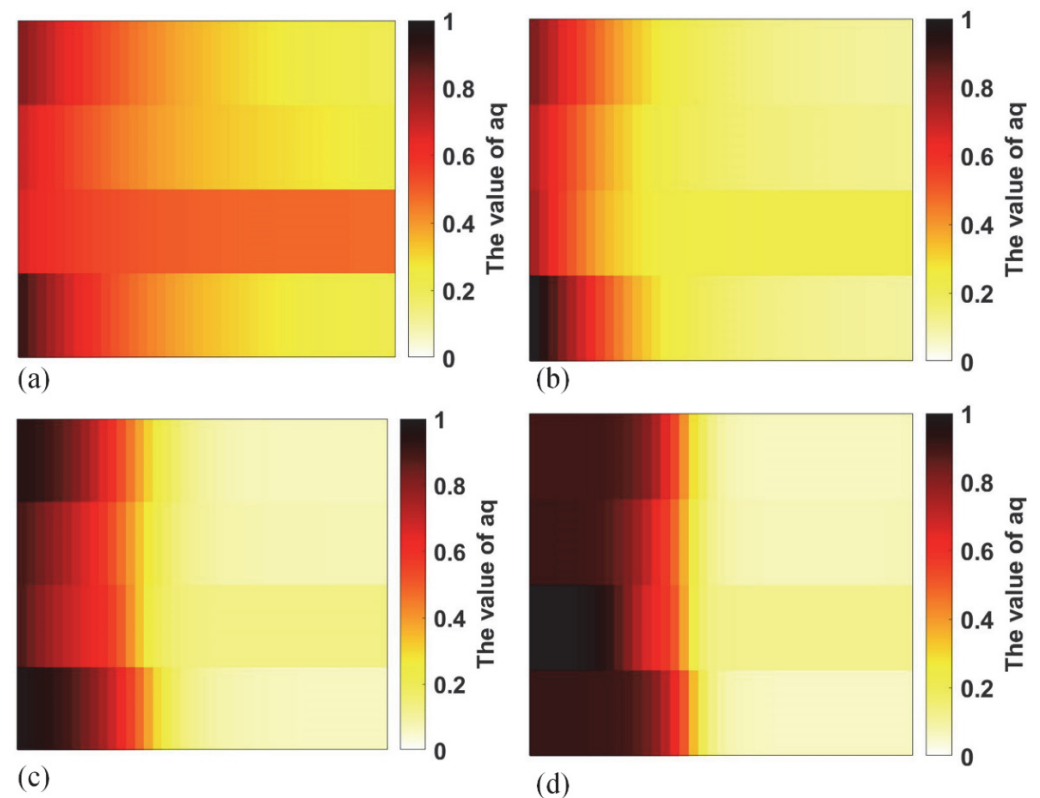

Figure 7. Chromaticity maps of $\alpha(q)$ with different q, (**a**) $q \in [-1, 1]$. (**b**) $q \in [-2, 2]$. (**c**) $q \in [-5, 5]$. (**d**) $q \in [-10, 10]$.

3.2. Recognition Results of Deep Learning Model

In this paper, the results are divided into four categories based on the ratio of strength values to initial strength values for ceramic materials in different cracking situations.

The obtained $\alpha(q)$ and $f(q)$ chromaticity maps were input into the model for training and the recognition accuracy of the model was tested using the test set. The test set recognition rates for different cases were obtained by adjusting the number of training rounds and the learning rate, as shown in Table 1.

To further improve the recognition rate, we varied the number of cuts in the $\alpha(q)$ and $f(q)$ chromaticity maps in both the longitudinal and transverse directions as a way to increase the availability of the characteristics of the spatial information distribution of the cracks. The chromaticity maps with six (Figure 8a) and eight (Figure 8b) additional vertical

cuts were identified in Table 2. Then, 15 copies of the image were cut horizontally (with partial overlap) in certain steps, and the identification results are shown in Table 3.

Table 1. Input the chromaticity diagram into the model and obtain the test set recognition rate under different training rounds and learning rates.

Learning Rate/Training Rounds	0.05/80	0.01/80	0.005/50	0.001/100
Chromaticity Diagram of $\alpha(q)$	60.28%	60.57%	60.23%	54.46%
Chromaticity Diagram of $f(q)$	64.13%	68.20%	67.27%	65.48%

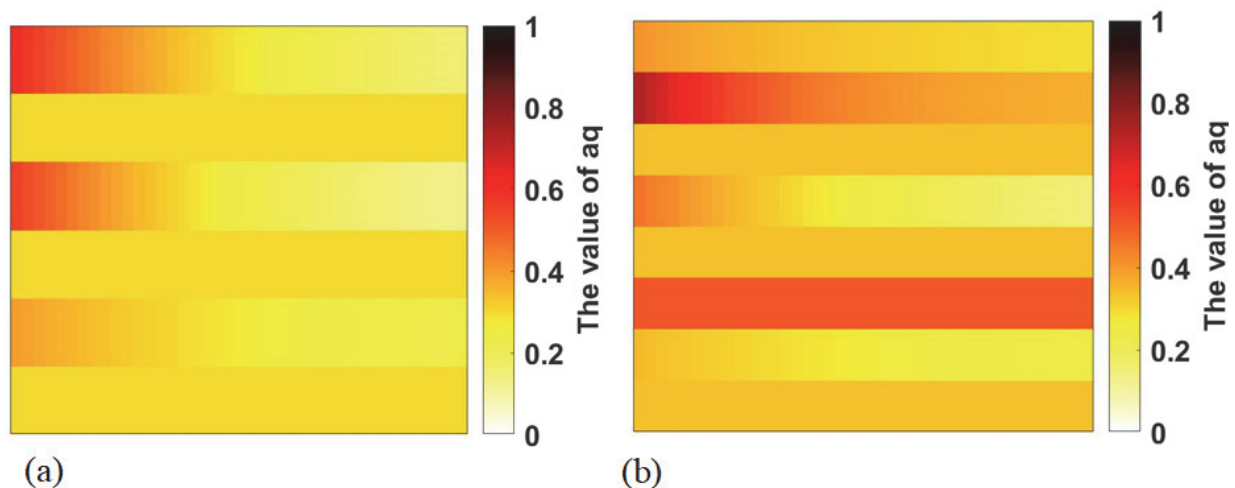Note: cutting for four rows and five columns.

Figure 8. Increase the number of cutting lines in the longitudinal direction to obtain its chromaticity diagram. (**a**) Cut six rows in the longitudinal direction. (**b**) Cut eight rows in the longitudinal direction.

Table 2. The test set recognition rate when cutting different numbers of rows.

Model	4-Line $\alpha(q)$	4-Line $f(q)$	6-Line $\alpha(q)$	6-Line $f(q)$	8-Line $\alpha(q)$	8-Line $f(q)$
Recognition Rate	61.39%	70.26%	75.20%	52.38%	73.82%	80.33%

Table 3. The image is cut horizontally at a certain step to enhance the data; test set recognition rate after data enhancement.

Model	4-Line $\alpha(q)$	4-Line $f(q)$	6-line $\alpha(q)$	6-Line $f(q)$	8-Line $\alpha(q)$	8-Line $f(q)$
Recognition Rate	62.50%	70.80%	79.16%	58.33%	75.00%	83.30%

Then, the post-processing method of model fusion was used to process the output of the deep learning model, and a voting mechanism was established. Multiple models were used to identify the image, and several models voted to get a relatively more correct result. The first was a probability-based model fusion method (Figure 9), where each model has a probability value for each of the four categories of an image, and the category with the highest probability is the result of recognition. The second method was the model fusion method based on the recognition results (Figure 10), where the recognition results of the six classes of chromaticity map models for one image are aggregated and the class with the highest number of recognitions is the final recognition result.

In this paper, the second method is used as a basis for designing a model fusion method applicable to this paper (Figure 11). The original image of the crack is input into a multifractal spectrum calculation model to obtain six types of chromaticity maps of the cracked image, and then these six types of maps are input into their respective

corresponding deep learning models to derive the recognition results of each model, and these results are voted on to derive the final recognition results. The final recognition rate was 87.5% using the test set for testing.
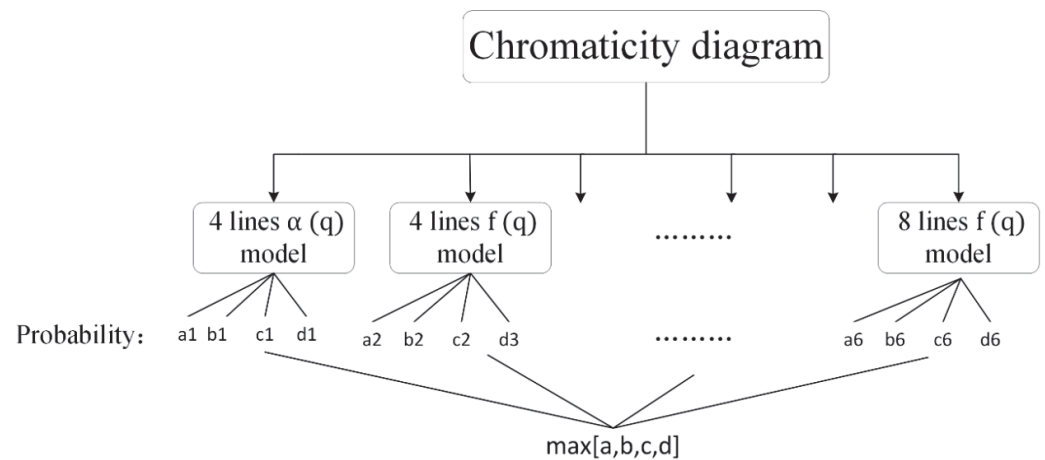

Figure 9. Add the corresponding probabilities to each category, and the category with the max. value is the recognition result.
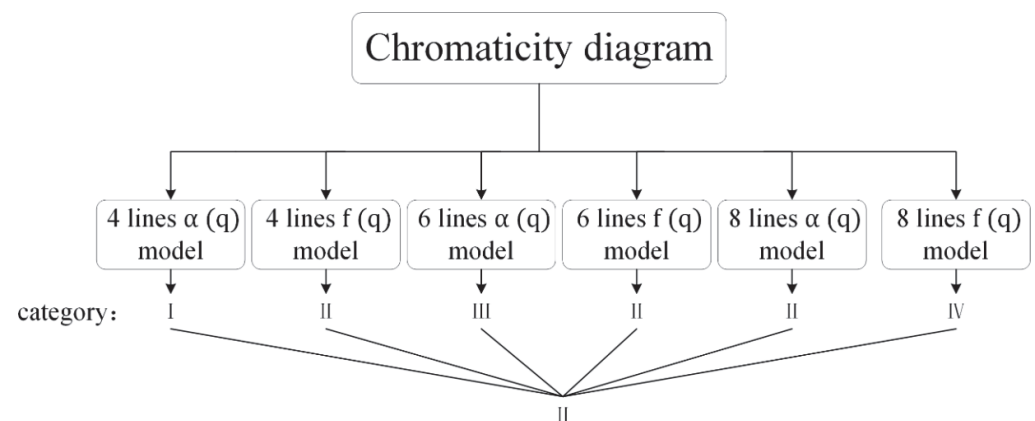

Figure 10. Each model obtains a recognition result, and the model with the highest votes reveals the final category.
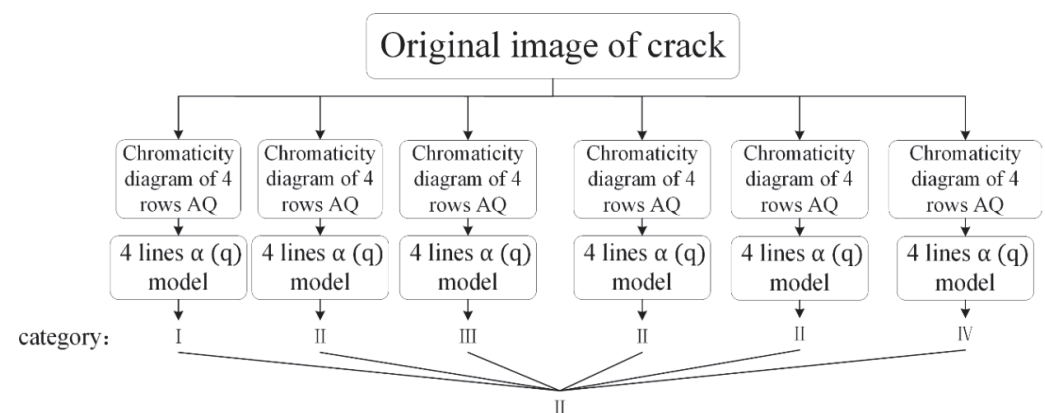

Figure 11. Improved fusion method.

4. Discussion

On account of its unique properties, the multifractal spectrum can provide a detailed description of surfaces with complex morphological conditions. In this paper, we characterize the complexity and self-similarity of crack images by calculating the multifractal

spectra of crack images, analyzing them from a fractal perspective, combining information on the spatial distribution of cracks with their non-linear characteristics, and converting each set of multifractal spectra into a chromaticity map to visualize the distribution pattern of cracks and the details of complex cracks.

By performing multifractal spectrum calculations on a large number of crack images and observing their chromaticity maps, it is found that the location, width, and bifurcation of the cracks affect the calculation results of the multifractal spectrum, which also verifies that even some minor features on the surface can be faithfully characterized by the multifractal. Based on the results of Qi [7], the fracture energy of microcrack fractal patterns in quasi-brittle solids can be used to explain the relationship between crack length and fractal dimension. If the crack propagation has the same crack length but a larger fractal dimension, it will absorb more energy. The relationship between the crack energy and the corresponding value of the singularity index, the singularity spectrum, can also be observed from the chromaticity diagram obtained in this paper.

The resulting chromaticity map was input into a deep learning model for training tests, and initially, the recognition accuracy peaked at 70.26%. By increasing the number of cut rows, enhancing the amount of data in the dataset, and model fusion, the recognition rate was increased to 87.50%.

In deep learning, evaluation metrics such as accuracy, precision, recall, and the F1-measure are generally used to evaluate a model. Table 4 shows the confusion matrix, where TP (True Positive), FP (False Positive), FN (False Negative), and TN (True Negative) are the number of samples in each case.

Table 4. Confusion matrix.

	The Sample is Actually Positive	**The Sample is Actually Negative**
The Sample Prediction is Positive	TP	FP
The Sample Prediction is Negative	FN	TN

The formulae for calculating each indicator are as follows [23]:

$$\text{Accuracy}: \ a = \frac{\text{TP} + \text{TN}}{\text{TP} + \text{TN} + \text{FP} + \text{FN}} \tag{6}$$

$$\text{Precision}: \ P = \frac{\text{TP}}{\text{TP} + \text{FP}} \tag{7}$$

$$\text{Recall}: \ R = \frac{\text{TP}}{\text{TP} + \text{FN}} \tag{8}$$

$$\text{F1} - \text{measure}: \ F1 = \frac{2 \times P \times R}{P + R} \tag{9}$$

These evaluation metrics are usually applied to dichotomous problems. For the multi-classification problems in this paper, both macro-averaging and micro-averaging methods are generally used to calculate each evaluation indicator.

This paper is a four-category problem, where each evaluation indicator P_i, R_i, and F1_i is first calculated for category i, where category i is treated as a positive category and the remaining categories as negative categories. The macro-average is calculated as follows [24]:

$$P_{mac} = \frac{P_1 + P_2 + P_3 + P_4}{4} \tag{10}$$

$$R_{mac} = \frac{R_1 + R_2 + R_3 + R_4}{4} \tag{11}$$

$$\text{F1}_{mac} = \frac{2 \times P_{mac} \times R_{mac}}{P_{mac} + R_{mac}} \tag{12}$$

The micro-average is calculated as follows [24]:

$$P_{mic} = \frac{\sum_{i=1}^{L} TP_i}{\sum_{i=1}^{L} TP_i + \sum_{i=1}^{L} FP_i} \tag{13}$$

$$R_{mic} = \frac{\sum_{i=1}^{L} TP_i}{\sum_{i=1}^{L} TP_i + \sum_{i=1}^{L} FN_i} \tag{14}$$

$$F1_{mic} = \frac{2 \times P_{mic} \times R_{mic}}{P_{mic} + R_{mic}} \tag{15}$$

Macro-averaging is essentially obtained by averaging the indicators, but this tends to ignore the uneven distribution between samples, which can be compensated for by micro-averaging. A combination of both macro-averaging and micro-averaging allows for a better evaluation of the model.

The final recognition accuracy of the deep learning model was 87.5%, through Equations (6)–(9), we calculated the evaluation indexes for each classification, then the macro-averaging and micro-averaging for each evaluation index are calculated by Equations (10)–(15), as shown in Table 5. From the evaluation indexes in the table, it can be seen that the evaluation indexes of the model are stable at 87.5%, so the model is reasonable and the results are in line with expectations. The evaluation indicators under the micro-average and macro-average are the same, and this shows that the data in the sample are well-distributed in all categories.

Table 5. Model evaluation index.

	Precision	Recall	F1-Measure
Mac	0.8875	0.8750	0.8812
Mic	0.8750	0.8750	0.8750

In this paper, multiple fractal spectroscopy is used to characterize cracks at the fractal level and extract crack features. At the same time, multiple fractal spectroscopy is combined with deep learning to achieve automatic recognition and classification of a large number of crack images and to improve their efficiency, accuracy, and repeatability. The chromaticity diagram of the singularity index and the singularity spectrum are obtained using the multiple fractal spectra, which, on the one hand, verifies that the relationship between the crack and fractal dimensions can be explained in terms of energy, and on the other hand, provides a data set for deep learning.

By combining multiple fractal spectroscopy with deep learning, a correlation model between microcrack propagation and thermal impact properties based on multifractal spectra and deep learning is constructed. A novel idea is developed in the study of material damage mechanisms. Crack features are extracted from the fractal level, and then the generalization ability of deep learning is used to transform the extracted features into scientific and reasonable data, to realize the final automatic classification and recognition.

5. Conclusions

This paper uses a combination of experimental evidence, multifractal theory, and deep learning to propose a characterization method for ceramic thermal shock cracks. A correlation model between microcrack propagation and thermal shock performance based on multifractal spectra and deep learning was constructed, which mainly leads to the following conclusions:

(1) Calculation of the multiple fractal spectra of different crack images, conversion of the values of the singularity index and singularity spectra in the multiple fractal spectra into chromaticity diagrams, verification of the relationship between the crack and fractal dimensions that can be explained from the energy point of view, and characterization of thermal shock cracks in ceramics from the fractal level are possible.

(2) The chromaticity map of thermal shock crack images obtained under different thermal shock temperatures was input into the deep learning model. The final recognition accuracy of the crack images was 87.50%, verifying that the model can effectively identify the class of its crack images under different propagation cases, improving the recognition accuracy of the crack images from the fractal level, highlighting the crack features, and extending the research on this kind of complex, non-uniform and non-linear geometric morphology. This provides new research ideas.

(3) This paper focuses on the classification and identification of static crack images. Future research can combine the crack propagation mechanisms to achieve the identification of the dynamic process of crack propagation, predict the crack propagation process, and monitor the health of materials and components in real time to enable targeted repair in advance, reduce costs and avoid accidents.

Author Contributions: Conceptualization, H.G.; Data curation, Y.S.; Funding acquisition, S.M. and F.Q.; Investigation, C.S.; Methodology, C.S., H.G. and S.X.; Project administration, F.Q.; Resources, Y.S.; Writing–original draft, C.S.; Writing–review and editing, H.G., S.W. and F.Q. All authors have read and agreed to the published version of the manuscript.

Institutional Review Board Statement: Not applicable.

Informed Consent Statement: Not applicable.

Data Availability Statement: Not applicable.

Conflicts of Interest: The authors declare no conflict of interest.

References

1. Dong, Y.L.; Wang, W.M. Progress of Investigation on Thermal Shock Resistance of Ceramic Materials. *Adv. Ceram.* **2004**, *1*, 37–41. [CrossRef]
2. Li, W.J.; Zhang, Y.; Zhang, X.H.; Hong, C.Q.; Han, W.B. Thermal Shock Behavior of ZrB2-SiC Ultra-high Temperature Ceramics with Addition of Zirconia. *J. Alloys Compd.* **2009**, *478*, 386–391. [CrossRef]
3. Griffith, A.A. The Phenomena of Rupture and Flow in Solids. *Philos. Trans. R. Soc. Lond.* **1921**, *221*, 163–198.
4. Duan, W.J.; Jia, D.C.; Cai, D.L.; Niu, B.; Yang, H.L.; Yang, Z.H.; Zhou, Y. Thermal shock damage assessment of a BNW/SiO2 ceramic: Insight from temperature-dependent material properties. *Ceram. Int.* **2021**, *47*, 19737–19742. [CrossRef]
5. Luo, J.T.; Wang, H.T.; Xi, C.Y.; Zhai, H.; Gu, Y.F.; Zhang, C.X. Indentation size effect–crack propagation model and finite element simulation verification for microhardness test of ceramic materials. *Ceram. Int.* **2021**, *47*, 4914–4924. [CrossRef]
6. Li, Y.Q.; Liu, B.Y.; Wang, X.H.; Shao, Y.F.; Li, L.; Wei, J.C.; Song, F. The effect of a prefabricated crack on the crack growth in ceramics during quenching. *Ceram. Int.* **2021**, *47*, 3643–3648. [CrossRef]
7. Qi, F.; Meng, S.H.; Song, F.; Guo, H.; Xu, X.H.; Shao, Y.F.; Chen, Y. Fractal characterization of ceramic crack patterns after thermal shocks. *J. Am. Ceram. Soc.* **2019**, *102*, 3641–3652. [CrossRef]
8. Ricco, P.; Ramos, N.C.; Campos, T.M.B.; Soares, V.O.; Boas, M.O.C.V.; Melo, R.M. The roles of microstructure and surface energy on subcritical crack growth in glass-ceramics. *Ceram. Int.* **2021**, *47*, 6827–6833. [CrossRef]
9. Quan, H.; Alderliesten, R.C. The energy dissipation during fatigue crack growth in metallic materials. *Eng. Fract. Mech.* **2022**, *269*, 108567. [CrossRef]
10. Quan, H.; Alderliesten, R.C. The energy dissipation during fatigue crack growth in adhesive joints under Mode-I loading. *Theor. Appl. Fract. Mech.* **2022**, *120*, 103418. [CrossRef]
11. Zhu, W.W.; Lei, G.; He, X.P.; Patzek, T.W.; Wang, M. Fractal and multifractal characterization of stochastic fracture networks and real outcrops. *J. Struct. Geol.* **2022**, *155*, 104508. [CrossRef]
12. Ji, Z.H.; Zhang, S.; Ma, X.; Ding, K.Y.; Chen, T.T. Phase Structure Characterization and High-speed Scraping Behavior Analysis of Abrasable Coatings Based on Multifractal. *Surf. Technol.* **2020**, *49*, 165–171. [CrossRef]

13. Pan, L.X.; Carrillo, J.L.; Cao, M.; Sha, G. Multifractal-spectrum shape parameters for characterizing distribution and evolution of multiple cracks in concrete structures. *Eng. Fract. Mech.* **2022**, *264*, 108329. [CrossRef]

14. Butenko, P.N.; Hilarov, V.L.B.A. Crystallization of $Ni_{50}Ti_{50}$ metallic glass ribbon in the concept of multifractal formalism. *Phase Transit.* **2022**, *95*, 537–550. [CrossRef]

15. Martsepp, M.; Laas, T.; Laas, K.; Priimets, J.; Mikli, V.; Antonov, M. Multifractal analysis of high-temperature plasma irradiated tungsten surfaces. *Surf. Topogr. Metrol. Prop.* **2021**, *9*, 035030. [CrossRef]

16. Feng, J.J.; Wang, E.Y.; Huang, Q.S.; Ding, H.C.; Dang, L. Time-varying Multifractal Analysis of Crack Propagation and Internal Fracture Process of Coal under Dynamic Loading. *Fractals* **2021**, *29*, 2150089. [CrossRef]

17. Jouini, M.S.; Bouchaala, F.; Riahi, M.K.; Sassi, M.; Abderrahmane, H.; Hjouj, F. Multifractal Analysis of Reservoir Rock Samples Using 3D X-Ray Micro Computed Tomography Images. *IEEE Access* **2022**, *10*, 67898–67909. [CrossRef]

18. Astinchap, B.; Ghanbaripour, H.; Amuzgar, R. Multifractal analysis of chest CT images of patients with the 2019 novel coronavirus disease (COVID-19). *Chaos Solitons Fractals* **2022**, *156*, 111820. [CrossRef]

19. Tsvetkov, V.P.; Mikheev, S.A.; Tsvetkov, I.V.; Derbov, V.L.; Gusev, A.A.; Vinitsky, S.I. Modeling the multifractal dynamics of COVID-19 pandemic. *Chaos Solitons Fractals* **2022**, *161*, 112301. [CrossRef]

20. Krizhevsky, A.; Sutskever, I.; Hinton, G.E. ImageNet classification with deep convolutional neural networks. *Commun. ACM* **2017**, *60*, 84–90. [CrossRef]

21. Li, M.; Li, J.; Xiong, X. Vibration discrimination based upon multifractal spectrum and improved probabilistic neural network in the dual Mach–Zehnder interferometric perimeter system. *Opt. Rev.* **2022**, *29*, 13–24. [CrossRef]

22. Xu, S.H.; Xia, M. Fractal Dimension and Multifractal Spectrum of Surface Morphology of Corroded Steel. *Mater. Rep.* **2020**, *34*, 16140–16143. [CrossRef]

23. Fawcett, T. An introduction to ROC analysis. *Pattern Recognit. Lett.* **2006**, *27*, 861–874. [CrossRef]

24. Shi, Z.W.; Liu, T.; Wu, G.Y. An Effective and Efficient Algorithm for Text Categorization. *Comput. Eng. Appl.* **2005**, *29*, 180–183.